chemosensors

MDPI

Article

Locally Enhanced Electric Field Treatment of *E. coli*: TEM, FT-IR and Raman Spectrometry Study

Irina Saraeva [1,*], Dmitry Zayarny [1], Eteri Tolordava [1], Alena Nastulyavichus [1], Roman Khmelnitsky [1], Dmitry Khmelenin [2], Svetlana Shelygina [1] and Sergey Kudryashov [1]

[1] P. N. Lebedev Physics Institute of Russian Academy of Sciences, 119991 Moscow, Russia; zayarniyda@lebedev.ru (D.Z.); tolordava.eteri@yandex.ru (E.T.); nastulyavichusaa@lebedev.ru (A.N.); khmelnitskyra@lebedev.ru (R.K.); shelyginasn@lebedev.ru (S.S.); kudryashovsi@lebedev.ru (S.K.)
[2] Institute of Crystallography, Branch of the Federal Scientific Research Centre "Crystallography and Photonics", Russian Academy of Sciences, 119333 Moscow, Russia; dirq@mail.ru
* Correspondence: saraevain@lebedev.ru

Abstract: In this paper, we report the study of the low-voltage locally enhanced electric field treatment (LEEFT) of *E. coli* bacteria via TEM analysis and FT-IR and Raman spectrometry. The formation of pores was confirmed by TEM, which revealed the membrane rupture along with the formation of precipitates in the membrane and the cell volume, and by photoluminescence spectra of propidium iodide dye. LEEFT results in the alternation of DNA and RNA structure, indicated by the change in its α-helical and β-helical forms, decrease and narrowing of the nucleic acids-related IR and Raman peaks. Membrane damage is illustrated by the ambiguous character after low-voltage exposure: several membrane fatty acids' peaks are broadening, while the others narrow, which indicates the overall change of the molecular bonds in their moiety, and may result from the rigidification during the shrinkage of the inner membrane and the increase in fluidity of the outer membrane. The corresponding fingerprints of cytochrome *c* and *bo*, located in the membrane or in the periplasm, on Raman spectra, reflect the arising changes in their structure and moiety. The observed changes were partially confirmed by TEM images, which indicate the dense precipitates' formation in the cell volume and membrane, as well as the cytoplasmic membrane shrinkage away from the outer membrane.

Keywords: LEEFT; electroporation; TEM; FT-IR spectrometry; Raman spectrometry

Citation: Saraeva, I.; Zayarny, D.; Tolordava, E.; Nastulyavichus, A.; Khmelnitsky, R.; Khmelenin, D.; Shelygina, S.; Kudryashov, S. Locally Enhanced Electric Field Treatment of *E. coli*: TEM, FT-IR and Raman Spectrometry Study. *Chemosensors* **2023**, *11*, 361. https://doi.org/10.3390/chemosensors11070361

Academic Editor: Jose Manuel Andrade

Received: 18 May 2023
Revised: 22 June 2023
Accepted: 24 June 2023
Published: 27 June 2023

1. Introduction

Electroporation (EP) is a method widely used in a plethora of applications. The formation of pores in the bacterial membrane allows extracting biomolecules [1,2], changing the genetics of microorganisms [3,4] and—which is most-needed in the growing resistivity of bacteria to common bactericides—implementing the non-thermal pasteurization and manufacturing water filters [5,6].

Each bacterial cell has a resting transmembrane potential [7,8], and the cell membrane, consisting of the lipid bilayer, is considered a capacitor. After the application of external voltage, charged ions on both sides of the bilayer move under electrophoretic force, and their redistribution results in the induced transmembrane potential formation. The dipoles in a lipid bilayer start reorienting, their phosphate head groups turning inwards to the stochastically formed nanopores, therefore stabilizing them and leading to membrane damage [1]. The critical values for reversible and irreversible non-thermal electroporation vary from cell to cell, depending on the microorganism type, temperature and pH of the medium, etc.; the reported values for irreversible EP reach several kV/cm [9].

One of the most effective types of electroporation is the pulsed electric field treatment (PEFT), which was successfully applied for inactivation of bacteria and bacterial spores [10–14]. Nevertheless, PEFT is a highly energy-consuming technique, often unsafe and accompanied by strong overheating, which may be inapplicable for some pur-

poses. An alternative variation of electroporation method is locally enhanced electric field treatment (LEEFT), which uses the functionalized surface, such as metal nanowires and nanofibers [15–19]. The resulting nanoscale surface roughness triggers the local electric field enhancement and lowers the needed critical value of applied external voltage for irreversible electroporation.

E. coli is a common food pathogen that may trigger severe diseases in the human organism [20]. Several works report the successful inactivation of *E. coli* by electroporation: Hup et al. [21] report the use of polydopamine-protected copper-phosphide nanowire-modified copper foam for water disinfection of *E. coli* cells; Liu et al. [22] have implemented the water sterilization by a nanosponge filtration system, based on the carbon nanotubes and Ag nanowires, which had resulted in a 2log inactivation of *E. coli*, *Salmonella enterica Typhimirium*, *Enterococcus faecalis*, and *Bacillus subtilis*. Xu et al. [23] have demonstrated the simultaneous destruction of *E. coli* by electroporation and its spectra acquisition via surface-enhanced Raman scattering (SERS), although the authors have used a chemical method of Au nanostructures' preparation with the use of $HAuCl_4$ and HF solution. The authors have also used an electrochemical cell for the electroporation and have demonstrated an increase in amide III and COO^- bands' intensity in the Raman spectra, which was suggested to result from the cytoplasm leakage due to membrane disruption.

In our previous work, we have successfully demonstrated the use of Au nanospikes for LEEFT-induced electroporation of *S. aureus* and *P. aeruginosa* [24], and in this paper we test the method on *E. coli* strain and study the emerging changes in the cells by means of FT-IR and Raman spectrometry, justifying the results with TEM and the standard microbiological tests. The additional numerical simulations and propidium iodide luminescence tests confirm the occurring electroporation, enrich the understanding of the electroporation method and illustrate the arising changes in *E. coli* bacterial cells.

2. Materials and Methods

2.1. Substrate Fabrication

Monocrystalline n-type silicon (Si) wafers (thickness 380 μm, area 10 × 20 mm^2) were covered by 230-nm gold (Au) films, magnetron-sputtered on both sides of the wafer in argon medium (SC7620, Quorum Technologies Lewes, Laughton, UK) with the use of silver or gold target (99.99% purity).

Radiation of an ytterbium-doped fiber laser (Satsuma, Amplitude systems, Pessac, France) with wavelength 1.03 μm, pulsewidth 300 fs and a galvanometric scanner ATECO with focus length of F-theta lens F = 160 mm was focused into a 10-μm spot, and an array of microcraters with area 5 × 5 mm^2 was written on the metal film surface at the constant scanning speed v_{scan} = 25 mm/s, pulse repetition rate f = 2 kHz, area filling of 0.05 lines/mm, average pulse energy E ≈ 2 μJ.

2.2. Bacterial Culture Preparation

Bacterial strains of *E. coli* 729 were obtained from the working collection of microorganisms of N.F. Gamaleya National Research Center for Epidemiology and Microbiology (Moscow, Russia). The clinical isolate is a producer of extended-spectrum beta-lactamases (ESBL) is resistant to cephalosporins of the 3rd–4th generation and to the polyvalent phage preparation "Piobacteriophage polyvalent" of the "Microgen" company (Ufa, Russia) and is sensitive to carbapenems. The overnight (18-h) culture was centrifuged with the subsequent removal of supernatant. The sedimented bacterial cells were intensively shaken with distilled water for 15 min, and the resulting suspension was diluted by subsequent decimal incubations up to 10^7 CFU/mL (colony-forming unit per milliliter).

2.3. Electroporation of Bacteria

A 10-μL drop of bacterial culture was placed on the electroactive substrate, secured in the holder, and the 10-V DC voltage was applied to the Au-coated silicon wafer through the spring-loaded copper contacts from the adjustable power supply ATH-3335 (Aktakom,

Eliks Ltd., Moscow, Russia), which corresponded to the current ~20 mA through the metal-semiconductor-metal transition.

2.4. Photoluminescence Spectra

For luminescence measurement, 3-µL of propidium iodide (PI) dye from the Live/Dead Viability Kit was diluted in 1 mL of distilled water. 8-µL drop of the diluted dye was placed on the air-dried electroporated samples and control (untreated) bacteria, and kept in the dark for 15 min. The excessive liquid was removed from the samples, and spectra of the PI dye luminescence were recorded with the excitation wavelength 520 nm, resulting in the emission maximum at ≈630 nm. All measurements were carried out with confocal scanning Raman micro-spectrometer Confotec-350 (Sol Instruments, Minsk, Belarus) in the range 500–700 nm.

2.5. Raman Spectrometry

The samples of *E. coli* bacteria before and after EP for Raman analysis were air-dried, and spectra were measured with the use of confocal scanning Raman micro-spectrometer Confotec-350 (Sol Instruments, Minsk, Belarus) with the excitation wavelength 520 nm with laser power 0.5 mW in the range 880–3090 cm^{-1}. Spectra for Raman bands' assignment were recorded in the full binning regime, with 3 sec accumulation time, exit slit width 2000 µm, pinhole width 100 µm, with a 40× objective lens (MPlanFL, Nikon, Tokyo, Japan) with a numerical aperture 0.75 and working distance 0.66 mm. All spectra were then smoothed by 20-point Savitzky-Golay method, baseline was corrected by asymmetric least squares smoothing with asymmetric factor 0.001, threshold 2×10^{-8}, smoothing factor 7, number of iterations 10. The spectra were normalized to the Phenylalanine band at 1001 [25,26].

2.6. FT-IR Spectrometry

The reflectance FT-IR spectra of the air-dried control and treated samples were recorded with the incident beam angle 14° in a vacuum chamber of V-70 (Bruker, Billerica, MA, USA) spectrometer. The 2-mm diaphragm was used, which allowed acquiring the spectra from the whole area of the sample. All spectra were recorded with a 4 nm step resolution (number of scans 128) in the range 400–8000 cm^{-1}. FT-IR reflectance spectra of *E. coli* before and after EP were corrected to the substrate (pure nanostructured Au film). All spectra were normalized to amide I band at 1654 cm^{-1} [27]. Baseline was corrected by anchor points finding by second derivative zeroes with smoothing window size 3 and threshold 0.05. IR bands detection was implemented by second derivative hidden peak search (positive direction) with Savitzky-Golay smoothing with polynomial order 2, points of window 20. All IR peaks were then fitted by Lorentzian approximation with fixed peak center values, deriving peak bandwidth and area values. All analysis was carried out using OriginPro 2019b 9.6.5.169 software.

2.7. SEM

The surface morphology of the substrate was analyzed by scanning electron microscope (SEM) TESCAN Vega (Tescan JSCo, Brno, Czech Republic), operating in this work at 15-keV electron beam energy.

2.8. TEM

The possible changes in bacterial cells' morphology were studied, using a transmission electron microscope (TEM) Tecnai G12 (FEI Company, Hillsboro, OR, USA), operating at an accelerating voltage of 200 keV. The bacterial cells from the substrates after electroporation were washed down in the saline, placed on a carbon-coated golden mesh and air-dried.

2.9. Numerical Simulation

Numerical simulation of the static electric field potential lateral distribution is based on the Dirichlet problem with boundary conditions as a defined constant electric field on the electrodes, magnetron-sputtered on both sides of Si substrate. There are no charged particles in the modelled 3D area, so the electric potential φ according to Laplass equation $\Delta\varphi = 0$. This problem is typical in the COMSOL Multiphysics software with module AC/DC. The electric currents in the model were low, so the arising magnetic fields were not accounted for. In order to optimize the modelling for nanostructured periodical metal film we have chosen a 20 × 20 µm computing cell with a 10-µm hole at the center of the metal film, which corresponded to the crater, formed after laser ablation. The height of the cell consisted of the height of the used silicon plate and the sputtered metal films, and equaled 380.52 µm. The cell was supplied by 150 µm water layer above the structured metal film surface with cross-section 60 × 60 µm. Electrical conductivity of the materials used in our model, such as Au film, sputtered on the Si substrate, and the distilled water layer, were defined by standard values in COMSOL Multiphysics 6.1 software ($45.6 \cdot 10^6$ S/m and $5.5 \cdot 10^{-6}$ S/m, correspondingly); dielectric susceptibility of water equaled 75 for the temperature 39 °C, electrical conductivity of the monocrystal n-type Si plate equaled 22.22 S/m. The electric field lateral distribution for the used cell, exposed to constant voltage 6.5 V, is presented in Figure 1. One can see that a heterogenous electric field is formed above the laser-modified metal film and field lines starting and closing on the surface of the film, so bacteria in the water layer above the nanostructured film, which has an electric charge, will be attracted to the film by Coulon force, regardless of the applied voltage polarity.

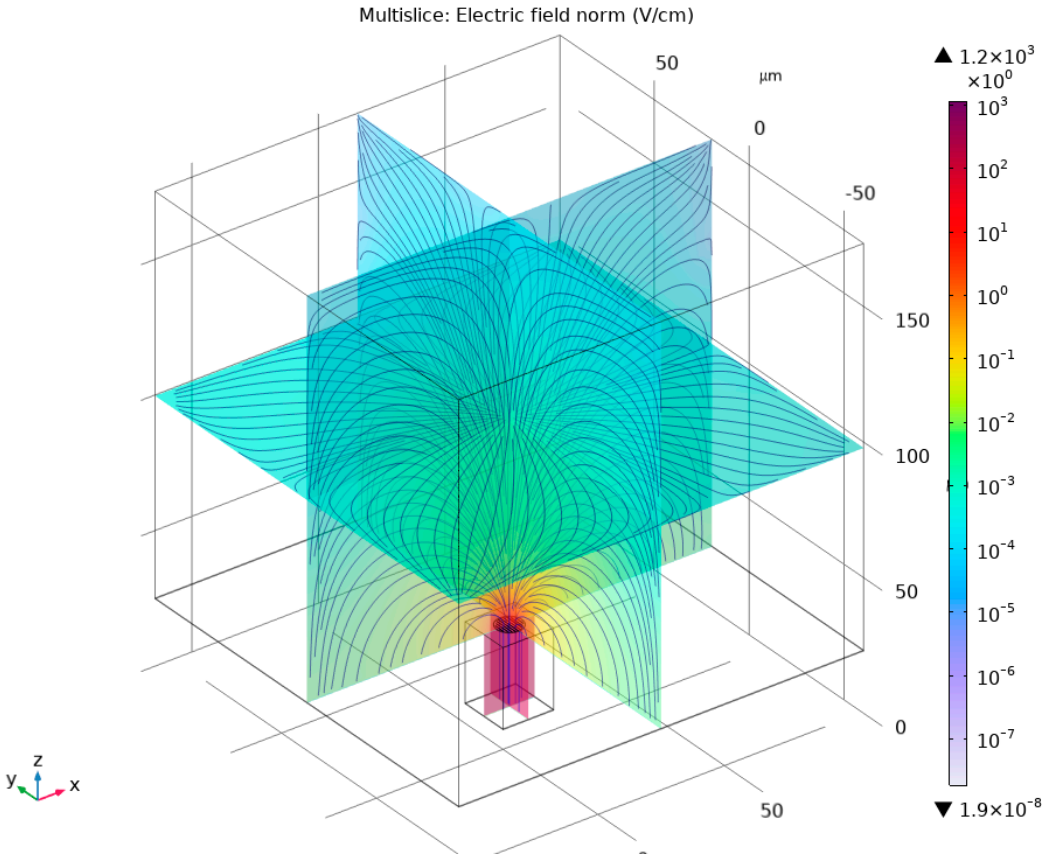

Figure 1. Numerical simulations of the electric field in a 3D model at the electrode voltage of 6.5 V.

3. Results and Discussion

3.1. Microbiological Tests

The bacterial population after electroporation equals 5×10^2 CFU/mL, with the control (untreated bacteria) 2×10^7 CFU/mL.

3.2. SEM, TEM and Photoluminescence Analysis

The mean size of surface nanoroughness, which fills the area of 10-µm crater, equals 10–100 nm (Figure 2a). The resulting relief is frequently observed during the spallation regime of femtosecond laser ablation [28], during which the sub-surface boiling leads to the formation of bubbles. Coagulation of these bubbles leads to the spallation of the melted layer in the form of nanoparticles.

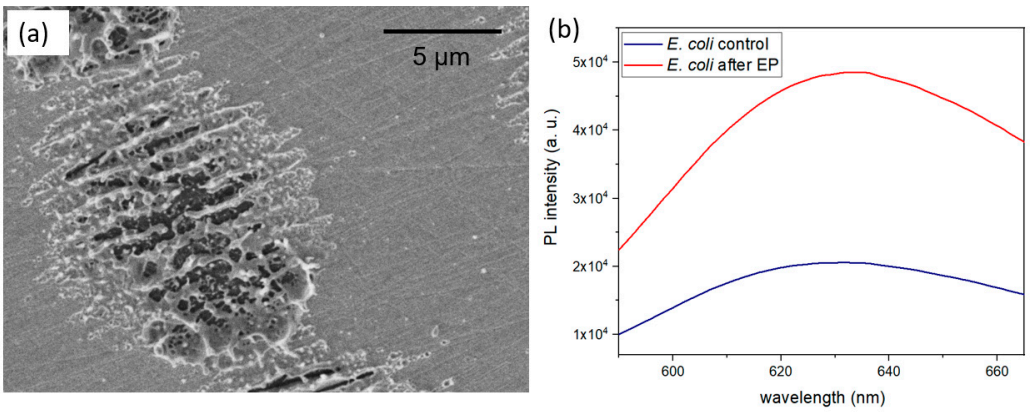

Figure 2. (**a**) SEM image of a single ablation crater on the surface of Au-coated Si substrate; (**b**) PI photoluminescence spectra of the dyed *E. coli* bacterial cells before (blue line) and after (red line) electroporation.

The resulting spectra of PI dye luminescence are presented in Figure 2b. Its excitation maximum locates at ≈535 nm, and fluorescence emission is maximum at ≈617 nm. Once the dye is bound to the DNA, its fluorescence is significantly enhanced, as can be seen in Figure 2b, which confirms the formation of the pores in the bacterial membranes.

The unchanged CFU/mL value for bacteria on the structured Au film without external voltage exposure indicates that the surface nanoroughness does not have an antibacterial effect. PI dye is able to penetrate only through pores >660 Da; therefore, in our work the emerging pores are bigger then ≈10 nm [29].

TEM analysis (Figure 3) revealed the formation of precipitates in the bacterial cells after EP. The untreated (control) bacterial cells are characterized by the homogenously distributed cell content, with intact membrane and clearly visible pili at the outside (Figure 3a,b). Electroporation results in the disfiguring of the membrane, leaving the cell in the "ghost-like" semi-transparent shell and misshaped. Rowan et al. interpret the similar arising changes in Bacillus cereus as the shrinkage of the cytoplasmic membrane away from the outer membrane [30]. The observed precipitates (dark spots in Figure 3c–e) may originate from the proteins' coagulation—both in the cell volume and in the membrane.

3.3. FT-IR Spectrometry

The resulting FT-IR optical density (OD) spectra of *E. coli* before and after EP are shown in Figure 4. Each IR peak parameter, acquired via Lorentz fitting (please see Section 2 for details), is presented in Table 1. Each table cell contains three rows, corresponding to the peak's spectral position (frequency, cm^{-1}), bandwidth and area (arbitrary units). For the peaks, which had not been detected during the fitting due to their low intensity, only spectral positions are presented, and their peculiarities are discussed in the text according to the second derivative graphs (Figure 5). The most significant changes are marked by bold font.

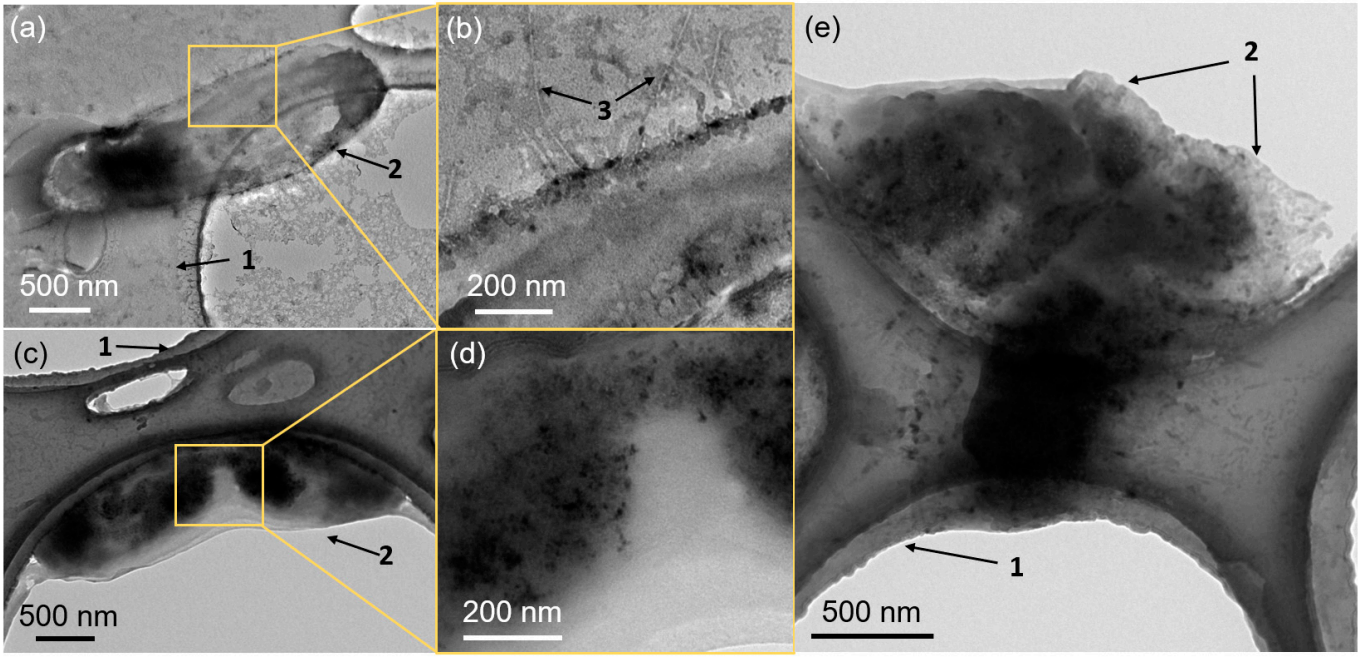

Figure 3. TEM images of *E. coli* bacteria before (**a**,**b**) and after (**c**–**e**) electroporation. 1—carbon-coated Au grid, used for the sample holding; 2—bacterial cells; 3—pili. (**b**,**d**)—the enlarged images of the selected areas (yellow boxes) in (**a**,**c**).

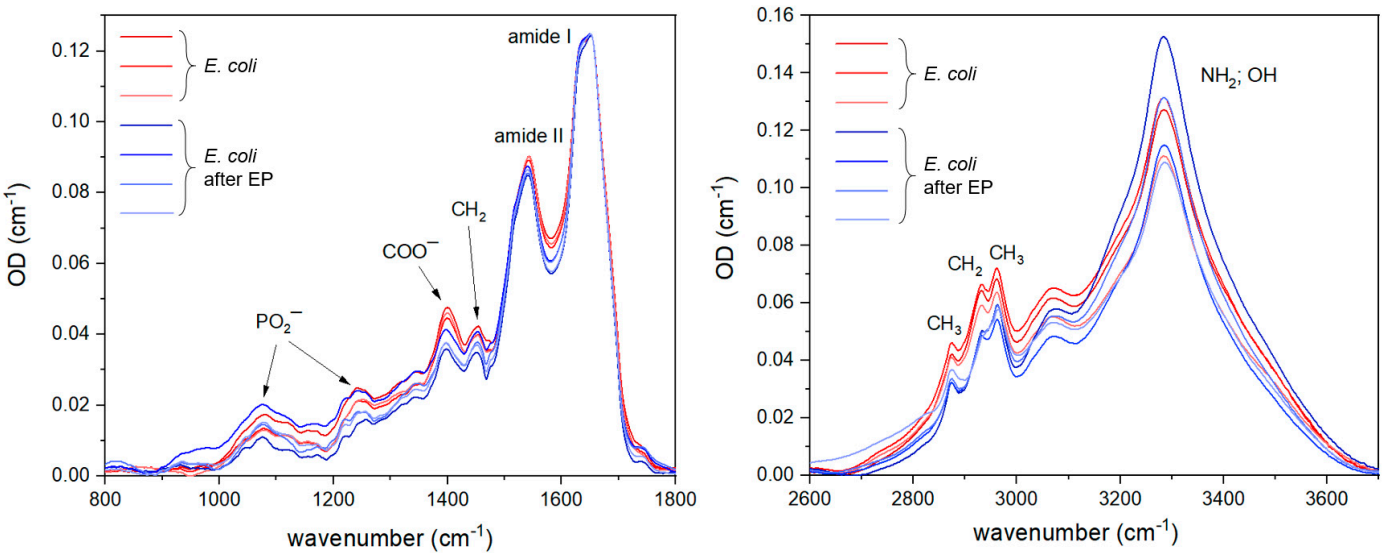

Figure 4. Normalized FT−IR spectra of *E. coli* on the nanostructured Au grid before (blue lines) and after electroporation (red lines).

E. coli is a Gram-negative bacterium, and its inner and outer membranes are separated by a layer of periplasmatic substance. Membrane components include lipopolysaccharides, containing phosphate and pyrophosphate groups [31]. Bacterial cells can vary the membrane fluidity in order to adjust to the stress in the environment (changes of pH, temperature, toxic compounds etc.). Such homeoviscous adaptation includes the change in the membrane fatty acids composition. In *E. coli*, adaptation causes the increase in the phospholipids' saturation degree. The discussion of the peculiarities in the FT-IR spectra was divided in terms of the cell components that are assigned to the given peaks: changes in the DNA, membrane and proteins.

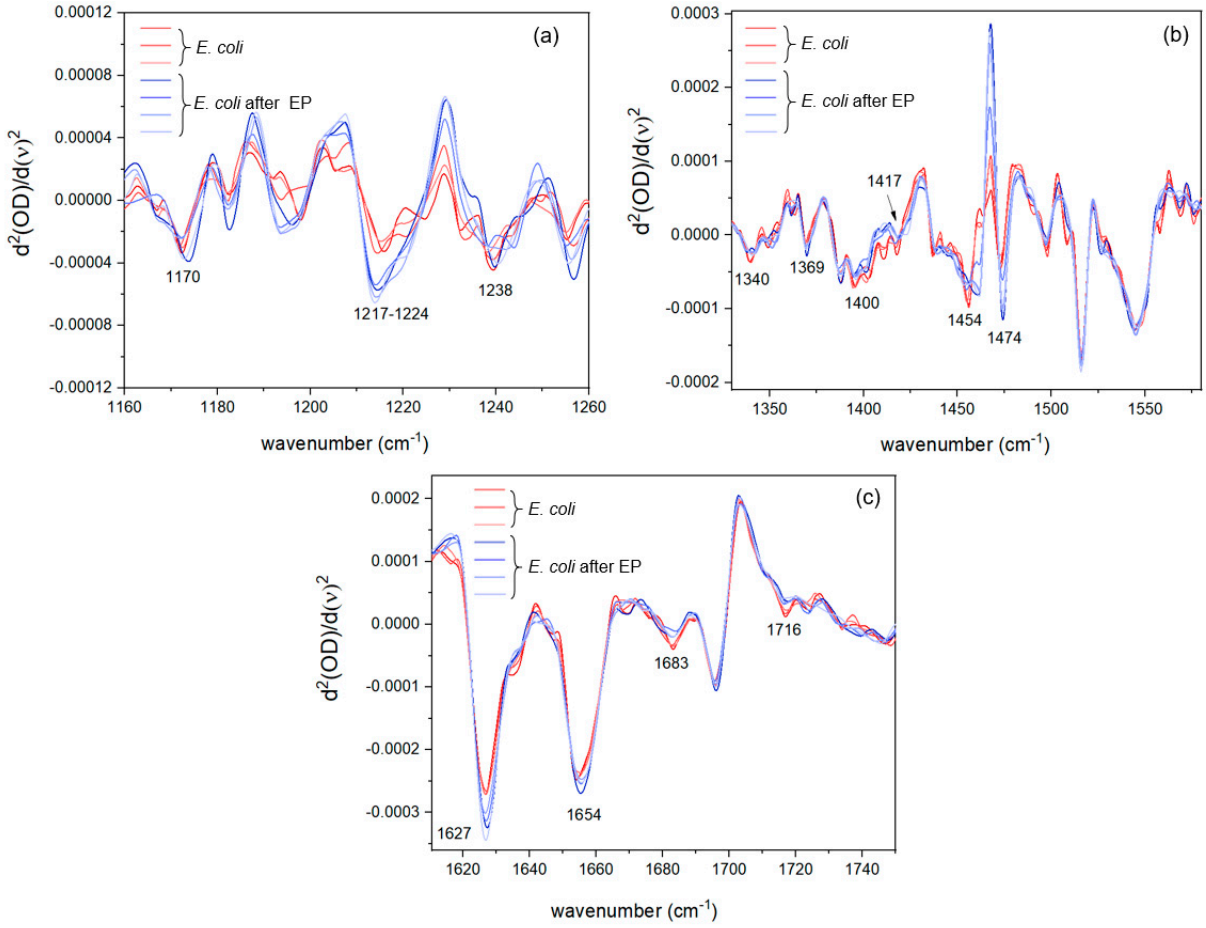

Figure 5. Selected regions of FT−IR second derivative spectra of *E. coli* on the nanostructured Au-coated Si substrate before (blue lines) and after (red lines) electroporation. (**a**) the region from 1160 to 1260 cm^{-1}; (**b**) from 1300 to 1600 cm^{-1}; (**c**) from 1610 to 1750 cm^{-1}.

DNA

The peak at 931 cm^{-1} corresponds to the C-O-C ring vibrations of deoxyribose in the DNA backbone [32,33]. The peaks at 963 cm^{-1}, 1127 cm^{-1} and 1417 cm^{-1} represent the C-O and C-O-H vibrations of DNA and RNA backbone [32,34–37]. The area of PO_2 peak at 1081 cm^{-1} decreases after electroporation (Figure 5). PO_2^- asymmetric stretching is characterized by peaks at 1222 cm^{-1} and 1240 cm^{-1} [37–39], with the peak at 1222 cm^{-1} corresponding to the β-helical and at 1240 cm^{-1}–α-helical forms of DNA [38]. A shoulder at 1222 cm^{-1} becomes less prominent after EP (Figure 5); therefore, one may suggest that the content of β-helical forms of DNA decreases.

The peak at 1716 cm^{-1} was assigned to the base pair vibrations (third strand guanines) in DNA [38,40]. The decrease in its intensity (Figure 5) may indicate the destruction of the DNA caused by EP.

Membrane

The membrane fluidity may be reduced after EP, which is usually accompanied by the lowered mobility of the acyl chains.

Peptidoglycan is presented in FT-IR spectra as a series of peaks at 1155 cm^{-1}, 1396 cm^{-1}, 1452 cm^{-1} (Figure 5, Table 2). The peak at 1396 cm^{-1}, corresponding to the carboxylate end COO^- (as) [41] in amino acids, fatty acids or side groups of peptidoglycan, shifts to lower frequency, and demonstrates a broadening, while the peak at 1452 cm^{-1} (CH_2) narrows, and its area decreases (Table 2), which may indicate the disruption of the molecular bonds in peptidoglycan and its partial rigidification [41–44].

The peak at 1010 cm^{-1}, according to the literature, may be assigned to the ether linkages [45], possibly in the N-acetylmuramic acid [46] in the cell wall.

Fatty acids in the membrane are presented by several peaks, assigned to the CH_2 vibrations: 1312 cm^{-1}, 1342 cm^{-1}, 2935 cm^{-1} [36,47–51] (Figure 5, Table 2). The peak at 1312 cm^{-1} exhibits strong narrowing and area decrease, while the peak at 2935 cm^{-1} broadens, and its area increases. CH_3 asymmetric stretching in fatty acids corresponds to the peaks at 2962 cm^{-1} and 3063 cm^{-1}, both shifting to higher wavenumbers and narrowing. The observed shift to higher wavenumbers may indicate an increase in hydrocarbon chain conformational disorder after the pore formation [52–54].

The overall inhomogeneous dynamics of the membrane fluidity may result from the observed inner membrane shrinkage and outer membrane destruction, observed in TEM images (Figure 3c–e), both deformations contributing to the FT-IR spectra variations.

Proteins

The band at 1515 cm^{-1} corresponds to the ring vibration in tyrosine [55,56]. Amide III vibrations' peak at 1288 cm^{-1} becomes more prominent (which may indicate its narrowing) after EP (Figure 4).

Table 1. FT-IR peak parameters before and after electroporation of *E. coli* bacteria. Each cell contains three lines, corresponding to peak frequency, bandwidth and area.

Functional Groups	Frequency, cm^{-1} Bandwidth, a. u. Area, a. u.	After EP
	Control	
C-O-C ring deoxyribose [32]	931.96 ± 0.21	932.34 ± 1.19
C-C, C-O deoxyribose in the DNA backbone [32,37]	963.15 ± 0.72	963.30 ± 1.09
C-O-C in ether linkages [45]	1010.89 ± 0.54	1010.73 ± 0.50
PO_2^- in nucleic acids and phospholipids [37,43]	1081.97 ± 1.09	1083.49 ± 0.34
C-C DNA and RNA backbones [32]	1127.83 ± 0.36	1128.88 ± 0.44
C-OH, C-O, C-O in amino acids peptidoglycan [36,43]	1155.01 ± 0.18	1154.57 ± 0.52
PO_2^- β-helical form of DNA [38,43]	1222.11 ± 2.21	1220.05 ± 1.06
PO_2^- α-helical nucleic acids [32,36,38]	1240.04 ± 0.01 55.24 ± 14.30 1.22 ± 0.55	1242.45 ± 0.96 62.50 ± 18.52 1.19 ± 0.66
Amide III (C-N coupled with N-H) [44] proteins	1288.10 ± 0.46	1287.79 ± 0.92
CH_2 in fatty acids [44]	**1312.36 ± 0.10** **102.31 ± 8.73** **2.75 ± 0.52**	**1318.14 ± 1.11** **74.63 ± 12.79** **1.5 ± 0.37**
CH_2 in fatty acids [47,48]	1342.25 16.99 ± 4.47 0.09 ± 0.05	1343.53 ± 1.11 16.66 ± 6.55 0.11 ± 0.07
CH_2 in fatty acids [48]	1369.39 ± 0.22	1369.30 ± 0.263
COO^- in amino acids, fatty acids or side groups of peptidoglycan [41]	**1396.25** **62.56 ± 1.95** **3.48 ± 0.29**	**1394.32** **74.62 ± 3.08** **3.32 ± 0.32**
C-O-H in-plane bending in the DNA/RNA backbone [35,36]	1417.29 ± 0.32	1417.96 ± 0.92

Table 1. *Cont.*

Functional Groups	Frequency, cm^{-1} Bandwidth, a. u. Area, a. u.	After EP
	Control	
C–H of CH_2 in lipids (peptidoglycan) [32,43]	**1452.18** **51.12 ± 0.98** **1.53 ± 0.10**	**1453.62 ± 0.96** **45.85 ± 3.99** **1.12 ± 0.15**
C-C of the tyrosine ring [55,56]	1515.82 43.61 ± 2.46 1.4 ± 0.22	1517.26 ± 0.96 45.11 ± 5.16 1.52 ± 0.31
Amide II N-H, C-N of proteins [32,36,44]	1544.26 ± 0.96 77.75 ± 1.49 8.58 ± 0.24	1543.30 ± 0.96 76.97 ± 1.13 7.97 ± 0.37
Amide I β-pleated sheets in proteins [55]	**1629.60** **61.99 ± 0.55** **5.31 ± 0.18**	**1629.60** **51.56 ± 1.66** **4.58 ± 0.47**
Amide I α-helices in proteins [55]	**1654.67** **62.99 ± 0.40** **8.78 ± 0.20**	**1655.15 ± 0.96** **56.92 ± 3.88** **8.28 ± 0.93**
Amide I β-pleated sheets in proteins [36]	1695.58 ± 0.17502	1695.80 ± 0.20
Base pair (Guanine) vibrations in DNA [38,40]	1716.96 ± 0.10	1716.98 ± 0.71
C=O in lipids and phospholipids [38,43]	1747.57 ± 0.86	1746.04 ± 1.63
C-H of CH_3 in proteins [36,43]	**2871.58** **104.03 ± 4.30** **4.94 ± 0.39**	**2871.58** **110.51 ± 2.93** **3.95 ± 0.07**
C-H of CH_2 in fatty acids [50,51]	**2935.22** **27.41 ± 0.03** **1.01 ± 0.06**	**2935.86 ± 1.11** **35.14 ± 5.51** **1.18 ± 0.37**
C-H in CH_3 of fatty acids [32,44]	**2962.22 ± 0.01** **37.07 ± 1.65** **1.88 ± 0.20**	**2964.15 ± 0.01** **36.96 ± 1.62** **1.72 ± 0.14**
C-H in CH_3 of fatty acids [32,44]	**3063.14 ± 1.11** **187.22 ± 14.32** **13.83 ± 1.05**	**3064.43** **147.95 ± 8.41** **9.07 ± 0.71**

Amide II vibrations are presented by the peak at 1544 cm^{-1}. The amide I peak at 1629 cm^{-1} narrows, and its area decreases.

The peak, corresponding to the CH_3 symmetric vibrations of membrane proteins (2871 cm^{-1}), broadens after the EP treatment, and its area decreases, which may indicate the disruption of protein structure and its content decrease.

3.4. Raman Spectrometry

Raman spectra are presented in Figure 6. The spectral positions of the bands and their assignment are presented in Table 2.

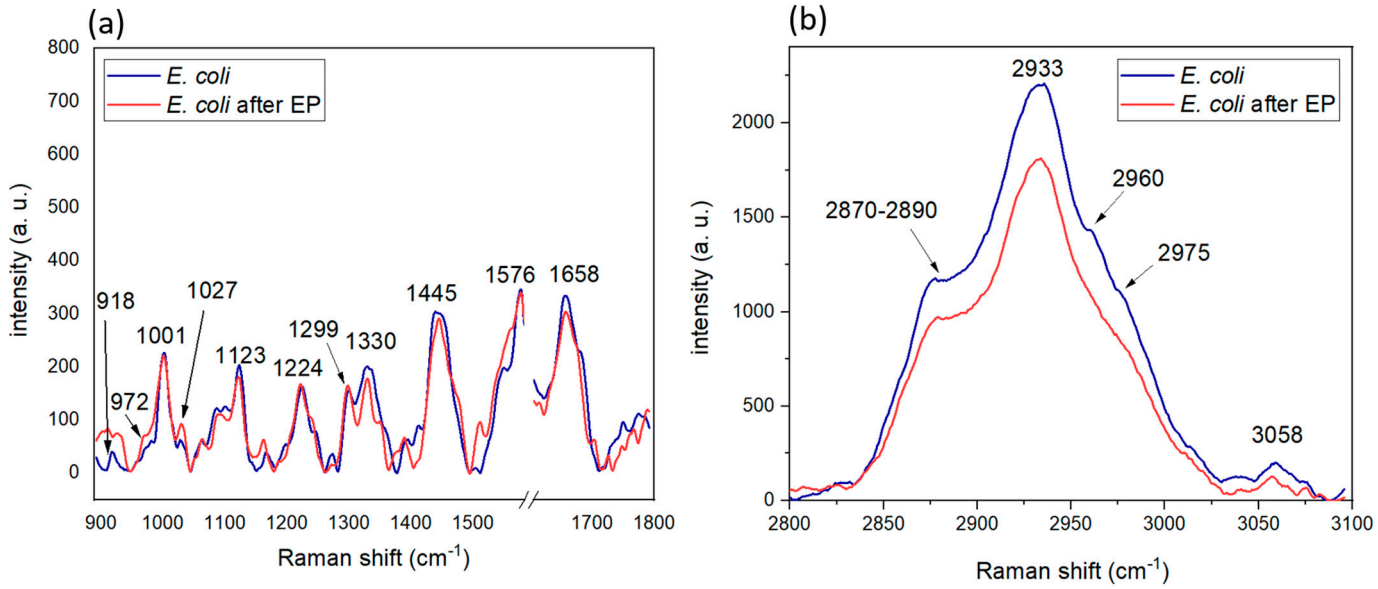

Figure 6. Selected regions of Raman spectra of *E. coli* bacteria before (blue lines) and after (red lines) electroporation with the marked positions of main peaks. (**a**) Region from 900 to 1800 cm^{-1}; (**b**) region from 2800 to 3100 cm^{-1}.

DNA

The band at 1085 cm^{-1}, assigned to the PO_2 stretching vibrations in nucleic acids [57], shifts to 1090 cm^{-1}, and its intensity lowers; this trend correlates with FT-IR data. Vibrational peak in DNA/RNA at 1330 cm^{-1} narrows, and its intensity decreases. Adenine (A) and guanine (G) molecular vibrations exhibit a shoulder at 1359 cm^{-1}, which disappears after the EP. Another peak, assigned to A and G at 1445 cm^{-1} narrows, its area decreasing; the peak at 1576 cm^{-1} also decreases (Figure 6, Table 2). In summary, the narrowing of the bands, along with overall intensity decrease, correlates with FT-IR data, and may result from the rigidification of the nucleic acids.

Membrane damage

Phospholipids are presented in the spectra as a peak at 1027 cm^{-1}, that shifts to 1030 cm^{-1}, broadens, and its intensity increases (Figure 6, Table 2). C-C chain stretching vibrations of cell wall lipids result in a peak at 1061 cm^{-1} [58], that broadens after EP. The peak at 1299 cm^{-1}, assigned to the CH_2 vibrations in saturated lipids, shifts to 1298 cm^{-1} and narrows, its intensity increasing. The band, originating from the CH_3 vibrations, at 1394 cm^{-1} shifts to 1388 cm^{-1} (Figure 6, Table 2). All the peaks at 2870–2890 cm^{-1}, 2933 cm^{-1}, 2960 cm^{-1}, 2975 cm^{-1}, assigned to CH_3 and CH_2 vibrations of fatty acids in the cell membrane, demonstrate the intensity decrease [59,60]. Moreover, the peak intensity ratio I_{1100}/I_{1123} provides the order/disorder extent of the conformation of the alkyl chain of lipids and represents the ratio of disorder/order conformations of the C-C bond vibration in the alkyl chains [61,62]. The hidden peaks' parameters were determined through the Lorentzian fitting and the hidden peak search by second derivative. The resulted ratios for *E. coli* before and after EP equals 0.51 ± 0.09 and 0.61 ± 0.03, which may indicate the increase in disorder/order ratios of alkyl chains and the membrane fluidity [61].

Carbohydrates

The peak, assigned to the C-C, C-O-C stretching vibrations in carbohydrates at 1099 cm^{-1} disappears after EP (Figure 6, Table 2).

Proteins

Skeletal stretching vibrations of COO-, C-C, result in the Raman peak at 918–926 cm^{-1} [57]. The peak at 1001 cm^{-1} corresponds to the Phe vibrations, and it increases, broadening.

CH_2, C-C vibrations, as well as α-helices contributions to the proteins, are assigned to the peak at 972 cm^{-1} [63], which broadens after EP. Phe is also presumably presented by the bands at 981 cm^{-1}, 1027 cm^{-1}, 1605 cm^{-1} and 3058 cm^{-1} [64]. The peak at 981 cm^{-1} degrades to a weak shoulder after EP. The peak at 1027 cm^{-1} shifts to 1030 cm^{-1}, broadens, and its intensity increases. The peak at 1605 cm^{-1} [65] broadens, and its intensity lowers. The peak at 3058 cm^{-1} shifts to 3057 cm^{-1} and its intensity decreases (Figure 6, Table 2).

The peak at 1123 cm^{-1} was assigned to cytochrome *c* [66]. This peak shifts to 1121 cm^{-1}, and its area decreases (Figure 6, Table 2). Cytochromes are proteins that are distributed in the cytoplasm or the periplasm, or are bound to the cytoplasmic membrane [67]. C-type cytochromes, specifically, are located on the periplasmic side of the cytoplasmic membrane [68]; therefore, the shift and the decrease in the band intensity at 1123 cm^{-1} may be caused by the disruption of the membrane. Cytochrome *bo* is also located in the membrane [69] and is usually presented by bands at 1476 cm^{-1} and 1503 cm^{-1} [70]. In our work, the more prominent shoulder at 1476 cm^{-1} appears only after EP, and the band at 1503 cm^{-1} shifts to 1510 cm^{-1}, its intensity drastically increasing (Figure 6, Table 2).

Aromatic amino acids in proteins present a peak at 1166 cm^{-1} [71], that shifts to 1161 cm^{-1} with an intensity increase. The amide III band shifts from 1224 cm^{-1} to 1221 cm^{-1}, and its area increases. The peak, originating from the amide III β-sheet at 1245 cm^{-1}, shifts to 1240 cm^{-1}, and its area increases. CH_2 stretching vibrations in amide III are presented by a peak at 1272 cm^{-1} that decreases after EP (Figure 6, Table 2). The amide II band at 1474 cm^{-1} appears after EP. Amide I 1658 cm^{-1} band narrows and decreases. Amide I 1681 cm^{-1} shoulder shifts to 1702 cm^{-1}. The peak at 3058 cm^{-1} was assigned to the C-H vibrations in the phenyl ring [64], and it shifts to 3057 cm^{-1}, its intensity decreasing.

C=C, N-H and C-N vibrations from amide II band, located at 1549 cm^{-1} [72,73], disappear after EP (Figure 6, Table 2). The peaks at 1658 cm^{-1} and 1681 cm^{-1} were assigned to amide I. The peak at 1658 cm^{-1} becomes narrower, and its intensity lowers; the peak at 1681 cm^{-1} appears as a shoulder in the Raman spectra and shifts to 1676 cm^{-1} after EP, its intensity decreasing.

As it was mentioned previously, Xu et al. [23] have demonstrated an increase in amide III and COO^- bands' intensity in Raman spectra, which was suggested to result from the cytoplasm leakage due to the membrane disruption. In our work, amide III bands at 1224 cm^{-1} and 1245 cm^{-1} also increase, although other proteins-related bands exhibit a decrease (peak at 1001 cm^{-1}, 1123 cm^{-1}, 1658 cm^{-1}, 3058 cm^{-1}) (Figure 6, Table 2). The membrane disruption may be partially vindicated by a decrease in the bands' intensities, related to cytochrome and membrane lipids. DNA/RNA-related bands demonstrate an overall decrease.

Table 2. Raman peaks' assignment before and after electroporation of *E. coli* bacteria.

Band Assignment	Frequency, cm^{-1} (Control)	Frequency, cm^{-1} (after EP)
Skeletal stretching COO-, C-C in proteins [57]	918–926	918–926
CH_2, C-C, α-helix in proteins [63]	972	972
C-C ring breathing in Phe in proteins [57]	981	-
Phe ring breathing, C-C skeletal in proteins [41,63]	1001	1001
δ(CH), Tyr, Phe aromatic compound in phospholipids/ carbohydrates [63]	1027	1030
C-C chain of cell wall lipids [41,58]	1061	1061
PO_2, (C-C), C-O Nucleic acid, lipid, carbohydrates [41,57]	1085	1090

Table 2. *Cont.*

Band Assignment	Frequency, cm^{-1} (Control)	Frequency, cm^{-1} (after EP)
C-C str, C-O-C in carbohydrates [41,57]	1100	1101
CH Cytochrome (proteins) [63,66]	1123	1121
Aromatic amino acids in proteins [71]	1166	1161
Amide III, adenine, polyadenine and DNA DNA/RNA [57,63]	1224	1221
Amide III β-sheet in proteins [57,58]	1245	1240
CH_2 str amide III in proteins [57]	1272	1272
CH_2 in saturated lipid [41,63]	1299	1298
NH_2 in A, polyadenine, C-H in DNA/RNA [57]	1330	1330
A, G, CH in nucleic acids, proteins [63]	1359	-
CH_3 in lipids [63]	1394	1388
COO- [66]	1411	-
G, A, C-H in nucleic acids, proteins, lipids, carbohydrates [63]	1445	1445
ν_3 band of heme in Cytochrome *bo* [63,70]	-	1476
ν_3 band of heme in Cytochrome *bo* [70]	1503	1510
N-H and C-N in amide II [57,70,73]	1549	-
G, A in nucleic acids [41,63]	1576	1576
Phe [41,65]	1605	1605
C=C, amide I envelope in proteins [57,63]	1658	1658
Amide I [41,57,58]	1681	1676
CH_2 [41]	2870–2890	2870–2890
CH_3 and CH_2 [41,59]	2933	2933
CH_2 in lipids [59,60]	2960	-
CH_3 [41]	2975	2975
CH in Phe [41,64]	3058	3057

3.5. Numerical Simulations

Numerical simulation of the lateral electric field with included objects imitating bacterial cells is of a particular interest. We have chosen *E. coli* as a model microorganism, which, according to the literature [74,75], can be presented as an ellipsoid with semi-axial radii of 0.4 and 1.5 μm. Its external coating with the width 20 nm has an electrical conductivity of 2 S/m, and its internal volume—0.33 S/m. Dielectric susceptibility of *E. coli* is taken as 80. During the calculations, the bacterial cell was placed on variable distances away from the nanostructured film, ranging from 5 nm to 100 μm, over both modified and smooth surfaces. Nanostructured areas in our model were presented as linear periodical grids with 1 μm period, which lie on the surface of Si plate and consist of Au lines with 100 × 100 nm cross-section with electric potential, equaling to the potential of the whole metal film.

An example of electric field lateral distribution calculation with a single bacterium under 6.5 V exposure is presented in Figure 7. When the bacterial cell was placed near the nanostructured film with normal distance several nm to 200 nm, a strong heterogeneous electric field was formed in the gap between bacterial cell and the charged film, with electric

field amplitude equaling to tens kV/cm. After the further distancing of bacterium by tens and hundreds of μm, the electric field of 3 to 10 kV/cm still existed adjacent to the cell, its value depending on the lateral orientation of the cell, which still exceeded the threshold for non-thermal irreversible electroporation [1]. This trend was applicable regardless of the bacterium position over the smooth or nanostructured area (Figure 8).

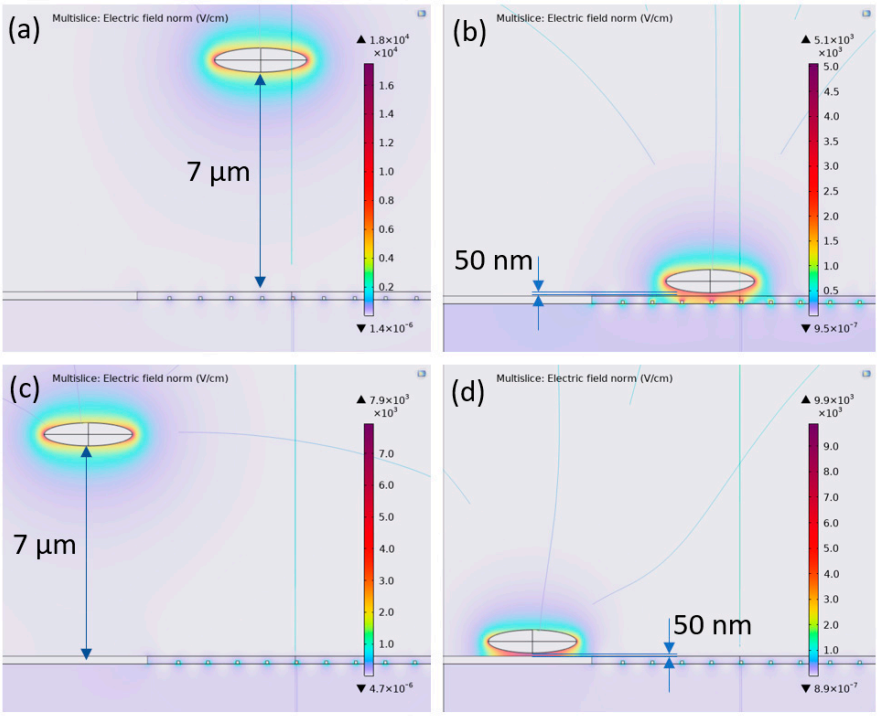

Figure 7. Electric field distribution and amplitude adjacent to *E. coli* bacterial cell with different distances between the cell and the nanostructured metal film: (**a**) bacterium 50 nm away from the smooth Au film; (**b**) bacterium 7 μm away from the smooth film; (**c**) bacterium 7 μm away from the structured film; (**d**) bacterium 50 nm away from the structured film.

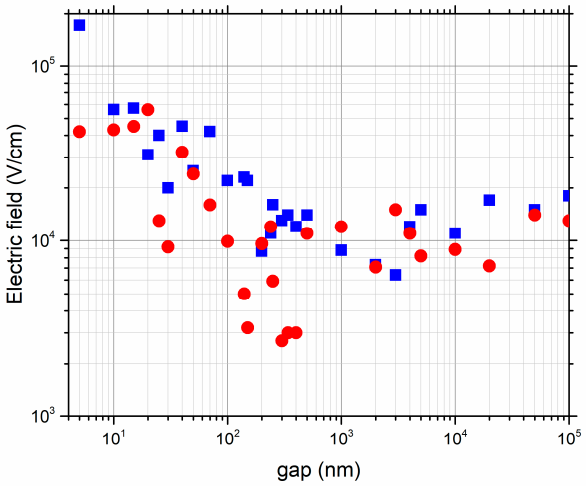

Figure 8. The dependence of maximal electric field value on the bacterial cell surface on the gap between the bacterium and the metal film. The lateral orientation of bacterium corresponds to the one in Figure 7. Blue squares—bacterium over nanostructured area of metal film; red circles—bacterium over the smooth area.

Thus, numerical simulations confirm the experimental results, stating the high bactericidal properties of the electroactive materials, which are explained by electroporation of the bacterial membrane.

4. Conclusions

In our work, we have studied the changes in the *E. coli* bacteria after low-voltage surface-enhanced electroporation via TEM analysis and FT-IR and Raman spectrometry. The formation of pores was confirmed by TEM, which revealed the rupture of the membrane and the formation of precipitates in the membrane and the cell volume, and by photoluminescence spectra of propidium iodide dye, which penetrated the cells through the formed pores. To summarize, the formation of pores during low-voltage application to *E. coli* results in several changes in the main components of the cell. We observed the arising changes in DNA and RNA structure, indicated by the change in α-helical and β-helical forms of DNA, decrease and narrowing of nucleic acids-related IR and Raman peaks. Membrane damage, caused by electroporation, is illustrated by the spectral characteristics' changes in the peaks, related to peptidoglycan, membrane lipids and proteins. Fatty acids in the membrane show an ambiguous character after low-voltage exposure: several peaks are broadening, while the others narrow, which indicates the overall change in molecular bonds in their moiety, and may result from the rigidification during the shrinkage of the inner membrane and the increase in fluidity of the outer membrane.

The fingerprints of cytochromes *c* and *bo*, which are located in the membrane or in the periplasm, on Raman spectra, also reflect the arising changes in the proteins' structure and moiety.

The observed changes were partially confirmed by TEM images, which indicate the formation of dense precipitates in the cell volume and membrane, as well as the shrinkage of the cytoplasmic membrane away from the outer membrane.

Author Contributions: Conceptualization, D.Z.; writing—original draft preparation, I.S. and D.Z.; experimental studies—D.Z., A.N. and I.S.; writing—review and editing, I.S., S.K., D.Z., E.T., A.N., S.S., D.K. and R.K.; microbiological tests, E.T.; SEM visualization, A.N. and S.S.; TEM visualization, D.K.; FT-IR analysis, R.K.; project administration, D.Z. All authors have read and agreed to the published version of the manuscript.

Funding: This research was funded by Russian Science Foundation, grant number 22-25-00185, https://rscf.ru/en/project/22-25-00185/ (accessed on 26 June 2023).

Institutional Review Board Statement: Not applicable.

Informed Consent Statement: Not applicable.

Data Availability Statement: The data presented in this study are available on request from the corresponding author.

Conflicts of Interest: The authors declare no conflict of interest.

References

1. Kotnik, T.; Frey, W.; Sack, M.; Meglič, S.H.; Peterka, M.; Miklavčič, D. Electroporation-based applications in biotechnology. *Trends Biotechnol.* **2015**, *33*, 480–488. [CrossRef] [PubMed]
2. Golberg, A.; Sheviryov, J.; Solomon, O.; Anavy, L.; Yakhini, Z. Molecular harvesting with electroporation for tissue profiling. *Sci. Rep.* **2019**, *9*, 15750. [CrossRef] [PubMed]
3. Somkuti, G.A.; Steinberg, D.H. Genetic transformation of Streptococcus thermophilus by electroporation. *Biochimie* **1988**, *70*, 579–585. [CrossRef] [PubMed]
4. Holo, H.; Nes, I.F. Transformation of Lactococcus by electroporation. *Electroporation Protoc. Microorg.* **1995**, *47*, 195–199. [CrossRef]
5. Tian, J.; Feng, H.; Yan, L.; Yu, M.; Ouyang, H.; Li, H.; Wang, Z.L. A self-powered sterilization system with both instant and sustainable anti-bacterial ability. *Nano Energy* **2017**, *36*, 241–249. [CrossRef]
6. Yu, D.; Liu, L.; Ding, B.; Yu, J.; Si, Y. Spider-Web-Inspired SiO2/Ag nanofibrous aerogels with superelastic and conductive networks for electroporation water disinfection. *Chem. Eng. J.* **2023**, *461*, 141908. [CrossRef]
7. Suzuki, H.; Wang, Z.Y.; Yamakoshi, M.; Kobayashi, M.; Nozawa, T. Probing the transmembrane potential of bacterial cells by voltage-sensitive dyes. *Anal. Sci.* **2003**, *19*, 1239–1242. [CrossRef]
8. Biener, G.; Masson-Meyers, D.S.; Bumah, V.V.; Hussey, G.; Stoneman, M.R.; Enwemeka, C.S.; Raicu, V. Blue/violet laser inactivates methicillin-resistant *Staphylococcus aureus* by altering its transmembrane potential. *J. Photochem. Photobiol. B Biol.* **2017**, *170*, 118–124. [CrossRef]

9. Yarmush, M.L.; Golberg, A.; Serša, G.; Kotnik, T.; Miklavčič, D. Electroporation-based technologies for medicine: Principles, applications, and challenges. *Annu. Rev. Biomed. Eng.* **2014**, *16*, 295–320. [CrossRef]
10. Schoenbach, K.H.; Joshi, R.P.; Stark, R.H.; Dobbs, F.C.; Beebe, S.J. Bacterial decontamination of liquids with pulsed electric fields. *IEEE Trans. Dielectr. Electr. Insul.* **2000**, *7*, 637–645. [CrossRef]
11. Pillet, F.; Formosa-Dague, C.; Baaziz, H.; Dague, E.; Rols, M.P. Cell wall as a target for bacteria inactivation by pulsed electric fields. *Sci. Rep.* **2016**, *6*, 19778. [CrossRef] [PubMed]
12. Siemer, C.; Toepfl, S.; Heinz, V. Inactivation of Bacillus subtilis spores by pulsed electric fields (PEF) in combination with thermal energy–I. Influence of process-and product parameters. *Food Control* **2014**, *39*, 163–171. [CrossRef]
13. Jin, Z.T.; Su, Y.; Tuhela, L.; Zhang, Q.H.; Sastry, S.K.; Yousef, A.E. Inactivation of Bacillus subtilis spores using high voltage pulsed electric fields. In *Pulsed Electric Fields in Food Processing*, 1st ed.; Barbosa-Canovas, G.V., Zhang, Q.H., Eds.; CRC Press: Boca Raton, FL, USA, 2019; pp. 167–181. [CrossRef]
14. Wu, W.J.; Chang, J. Inactivation of vegetative cells, germinated spores, and dormant spores of *Bacillus atrophaeus* by pulsed electric field with fixed energy input. *J. Food Process Eng.* **2022**, *45*, e13959. [CrossRef]
15. Zhou, J.; Yu, C.; Wang, T.; Xie, X. Development of nanowire-modified electrodes applied in the locally enhanced electric field treatment (LEEFT) for water disinfection. *J. Mater. Chem. A* **2020**, *8*, 12262–12277. [CrossRef]
16. Pi, S.Y.; Sun, M.Y.; Zhao, Y.F.; Chong, Y.X.; Chen, D.; Liu, H. Electroporation-coupled electrochemical oxidation for rapid and efficient water disinfection with Co_3O_4 nanowire arrays-modified graphite felt electrodes. *Chem. Eng. J.* **2022**, *435*, 134967. [CrossRef]
17. Wang, T.; Brown, D.K.; Xie, X. Operando investigation of locally enhanced electric field treatment (LEEFT) harnessing lightning-rod effect for rapid bacteria inactivation. *Nano Lett.* **2021**, *22*, 860–867. [CrossRef] [PubMed]
18. Kumar, P.; Dhar, A.; Vaish, R. Hand-powered and portable water disinfection system by locally enhanced electric field treatment (LEEFT) with modified nanowire electrodes. *Eur. Phys. J. Plus* **2022**, *137*, 709. [CrossRef]
19. Pi, S.Y.; Wang, Y.; Lu, Y.W.; Liu, G.L.; Wang, D.L.; Wu, H.M.; Liu, H. Fabrication of polypyrrole nanowire arrays-modified electrode for point-of-use water disinfection via low-voltage electroporation. *Water Res.* **2021**, *207*, 117825. [CrossRef] [PubMed]
20. Allocati, N.; Masulli, M.; Alexeyev, M.F.; Di Ilio, C. *Escherichia coli* in Europe: An overview. *Int. J. Environ. Res. Public Health* **2013**, *10*, 6235–6254. [CrossRef]
21. Huo, Z.Y.; Liu, H.; Wang, W.L.; Wang, Y.H.; Wu, Y.H.; Xie, X.; Hu, H.Y. Low-voltage alternating current powered polydopamine-protected copper phosphide nanowire for electroporation-disinfection in water. *J. Mater. Chem. A* **2019**, *7*, 7347–7354. [CrossRef]
22. Liu, C.; Xie, X.; Zhao, W.; Liu, N.; Maraccini, P.A.; Sassoubre, L.M.; Cui, Y. Conducting nanosponge electroporation for affordable and high-efficiency disinfection of bacteria and viruses in water. *Nano Lett.* **2013**, *13*, 4288–4293. [CrossRef]
23. Xu, J.; Qu, K.; Zhao, J.; Jian, X.; Gao, Z.; Xu, J.; Song, Y.Y. In situ monitoring of the "point discharge" induced antibacterial process by the onsite formation of a Raman probe. *Anal. Chem.* **2019**, *92*, 2323–2330. [CrossRef] [PubMed]
24. Saraeva, I.N.; Zayarny, D.A.; Tolordava, E.R.; Nastulyavichus, A.A.; Khaertdinova, L.F.; Kudryashov, S.I.; Gonchukov, S.A. Electroactive nanostructured antibacterial materials. *Las. Phys. Lett.* **2022**, *19*, 085601. [CrossRef]
25. Rangan, S.; Kamal, S.; Konorov, S.O.; Schulze, H.G.; Blades, M.W.; Turner, R.F.; Piret, J.M. Types of cell death and apoptotic stages in Chinese Hamster Ovary cells distinguished by Raman spectroscopy. *Biotechnol. Bioeng.* **2018**, *115*, 401–412. [CrossRef] [PubMed]
26. Khmaladze, A.; Ganguly, A.; Kuo, S.; Raghavan, M.; Kainkaryam, R.; Cole, J.H.; Morris, M.D. Tissue-engineered constructs of human oral mucosa examined by Raman spectroscopy. *Tissue Engin. Part C Methods* **2013**, *19*, 299–306. [CrossRef]
27. Kansiz, M.; Billman-Jacobe, H.; McNaughton, D. Quantitative determination of the biodegradable polymer poly (β-hydroxybutyrate) in a recombinant *Escherichia coli* strain by use of mid-infrared spectroscopy and multivariative statistics. *Appl. Env. Microbiol.* **2000**, *66*, 3415–3420. [CrossRef] [PubMed]
28. Zhakhovskii, V.V.; Inogamov, N.A.; Petrov, Y.V.; Ashitkov, S.I.; Nishihara, K. Molecular dynamics simulation of femtosecond ablation and spallation with different interatomic potentials. *Appl. Surf. Sci.* **2009**, *255*, 9592–9596. [CrossRef]
29. Pagan, R.; Mañas, P. Fundamental aspects of microbial membrane electroporation. In *Pulsed Electric Fields Technology for the Food Industry: Fundamentals and Applications*, 1st ed.; Raso, J., Heinz, V., Eds.; Springer: Boston, MA, USA, 2006; pp. 73–94. [CrossRef]
30. Rowan, N.J.; Macgregor, S.J.; Anderson, J.G.; Fouracre, R.A.; Farish, O. Pulsed electric field inactivation of diarrhoeagenic Bacillus cereus through irreversible electroporation. *Lett. Appl. Microbiol.* **2000**, *31*, 110–114. [CrossRef]
31. Nikaido, H.; Nakae, T. The outer membrane of Gram-negative bacteria. *Adv. Microb. Physiol.* **1980**, *20*, 163–250. [CrossRef]
32. Wang, Y.; Zhou, Q.; Li, B.; Liu, B.; Wu, G.; Ibrahim, M.; Sun, G. Differentiation in MALDI-TOF MS and FTIR spectra between two closely related species *Acidovorax oryzae* and *Acidovorax citrulli*. *BMC Microbiol.* **2012**, *12*, 182. [CrossRef]
33. Kochan, K.; Lai, E.; Richardson, Z.; Neth-ercott, C.; Peleg, A.Y.; Heraud, P.; Wood, B.R. Vibrational spectroscopy as a sensitive probe for the chemistry of intraphase bacterial growth. *Sensors* **2020**, *20*, 3452. [CrossRef] [PubMed]
34. Muntean, C.M.; Lapusan, A.; Mihaiu, L.; Stefan, R. Strain dependent UV degradation of *Escherichia coli* DNA monitored by Fourier transform infrared spectroscopy. *J. Photochem. Photobiol. B Biol.* **2014**, *130*, 140–145. [CrossRef] [PubMed]
35. Socrates, G. *Infrared and Raman Characteristic Group Frequencies: Tables and Charts*; John Wiley Sons: Hoboken, NJ, USA, 2004.
36. Yu, C.; Irudayaraj, J. Spectroscopic characterization of microorganisms by Fourier transform infrared microspectroscopy. *Biopolym. Orig. Res. Biomol.* **2005**, *77*, 368–377. [CrossRef]

37. Gupta, A.D.; Karthikeyan, S.; Chitra, A. Resistance mechanism of Ni^{2+} ion individually and in combination with the Cr^{6+} ion in Staphylococcus aureus species to characterize the molecular changes studied using infrared spectroscopy coupled with chemometrics. *Infrared Phys. Technol.* **2018**, *94*, 126–133. [CrossRef]
38. Bumah, V.V.; Aboualizadeh, E.; Masson-Meyers, D.S.; Eells, J.T.; Enwemeka, C.S.; Hirschmugl, C.J. Spectrally resolved infrared microscopy and chemometric tools to reveal the interaction between blue light 470 nm, and methicillin-resistant *Staphylococcus aureus*. *J. Photochem. Photobiol. B Biol.* **2017**, *167*, 150–157. [CrossRef]
39. Singh, S.; Kumar, V.; Singla, S.; Sharma, M.; Singh, D.P.; Prasad, R.; Singh, J. Kinetic study of the biodegradation of acephate by indigenous soil bacterial isolates in the presence of humic acid and metal ions. *Biomolecules* **2020**, *10*, 433. [CrossRef]
40. Banyay, M.; Sarkar, M.; Gräslund, A. A library of IR bands of nucleic acids in solution. *Biophys. Chem.* **2003**, *104*, 477–488. [CrossRef]
41. Maquelin, K.; Kirschner, C.; Choo-Smith, L.P.; van den Braak, N.; Endtz, H.P.; Naumann, D.; Puppels, G.J. Identification of medically relevant microorganisms by vibrational spectroscopy. *J. Microbiol. Methods* **2002**, *51*, 255–271. [CrossRef]
42. Kamnev, A.A.; Antonyuk, L.P.; Tugarova, A.V.; Tarantilis, P.A.; Polissiou, M.G.; Gardiner, P.H.E. Fourier transform infrared spectroscopic characterisation of heavy metal-induced metabolic changes in the plant-associated soil bacterium *Azospirillum brasilense* Sp7. *J. Mol. Struct.* **2002**, *610*, 127–131. [CrossRef]
43. Cagnasso, M.; Boero, V.; Franchini, M.A.; Chorover, J. ATR-FTIR studies of phospholipid vesicle interactions with α-FeOOH and α-Fe_2O_3 surfaces. *Colloids Surf. B* **2010**, *76*, 456–467. [CrossRef]
44. Quilès, F.; Humbert, F.; Delille, A. Analysis of changes in attenuated total reflection FTIR fingerprints of *Pseudomonas fluorescens* from planktonic state to nascent biofilm state. *Spec. Act. Part A Mol. Biomol. Spec.* **2010**, *75*, 610–616. [CrossRef]
45. Ramteke, C.; Chakrabarti, T.; Saran-gi, B.K.; Pandey, R.A. Synthesis of silver nanoparticles from the aqueous extract of leaves of *Ocimum sanctum* for enhanced antibacterial activity. *J. Chem.* **2013**, *2013*, 278925. [CrossRef]
46. Jaeger, T.; Mayer, C. N-acetylmuramic acid 6-phosphate lyases (MurNAc etherases): Role in cell wall metabolism, distribution, structure, and mechanism. *Cell. Mol. Life Sci.* **2008**, *65*, 928–939. [CrossRef] [PubMed]
47. Hu, X.J.; Liu, Z.X.; Wang, Y.D.; Li, X.L.; Hu, J.; Lü, J.H. Synchrotron FTIR spectroscopy reveals molecular changes in *Escherichia coli* upon Cu^{2+} exposure. *Nucl. Sci. Tech.* **2016**, *27*, 56. [CrossRef]
48. Lewis, R.N.; McElhaney, R.N.; Monck, M.A.; Cullis, P.R. Studies of highly asymmetric mixed-chain diacyl phosphatidylcholines that form mixed-interdigitated gel phases: Fourier transform infrared and 2H NMR spectroscopic studies of hydrocarbon chain conformation and orientational order in the liquid-crystalline state. *Biophys. J.* **1994**, *67*, 197–207. [CrossRef]
49. Jiang, G.; Qiao, J.; Hong, F. Application of phosphoric acid and phytic acid-doped bacterial cellulose as novel proton-conducting membranes to PEMFC. *Int. J. Hydrogen Energy* **2012**, *37*, 9182–9192. [CrossRef]
50. Beekes, M.; Lasch, P.; Naumann, D. Anal. applications of Fourier transform-infrared FT-IR, spectroscopy in microbiology and prion research. *Vet. Microbiol.* **2007**, *123*, 305–319. [CrossRef]
51. Saulou, C.; Jamme, F.; Girbal, L.; Maranges, C.; Fourquaux, I.; Cocaign-Bousquet, M.; Mercier-Bonin, M. Synchrotron FTIR microspectroscopy of *Escherichia coli* at single-cell scale under silver-induced stress conditions. *Anal. Bioanal. Chem.* **2013**, *405*, 2685–2697. [CrossRef]
52. Kardas, M.; Gozen, A.G.; Severcan, F. FTIR spectroscopy offers hints towards widespread molecular changes in cobalt-acclimated freshwater bacteria. *Aquat. Toxicol.* **2014**, *155*, 15–23. [CrossRef]
53. Severcan, F. Vitamin E decreases the order of the phospholipid model membranes in the gel phase: An FTIR study. *Biosci. Rep.* **1997**, *17*, 231–235. [CrossRef]
54. Liu, K.Z.; Bose, R.; Mantsch, H.H. Infrared spectroscopic study of diabetic platelets. *Vib. Spectrosc.* **2002**, *28*, 131–136. [CrossRef]
55. Fabian, H.; Mäntele, W. Infrared spectroscopy of proteins. In *Handbook of Vibrational Spectroscopy*; John Wiley Sons: Hoboken, NJ, USA, 2006. [CrossRef]
56. Sukumaran, S.; Hauser, K.; Rauscher, A.; Mäntele, W. Thermal stability of outer membrane protein porin from *Paracoccus denitrificans*: FT-IR as a spectroscopic tool to study lipid–protein interaction. *FEBS Lett.* **2005**, *579*, 2546–2550. [CrossRef]
57. Bashir, S.; Nawaz, H.; Majeed, M.I.; Mohsin, M.; Abdullah, S.; Ali, S.; Abdulraheem, A. Rapid and sensitive discrimination among carbapenem resistant and susceptible *E. coli* strains using Surf. Enhanced Raman Spectroscopy combined with chemometric tools. *Photodiagn. Photodyn. Ther.* **2021**, *34*, 102280. [CrossRef]
58. Zheng, D.W.; Liu, X.Y.; Zhang, P.; Su, L.; Wang, L.M.; Wei, X.D.; Lin, T.F. Rapid identification of mixed enteropathogenic bacteria by means of Au nanoparticles@ bacteria using portable Raman spectrometer. *J. Nanosci. Nanotechnol.* **2018**, *18*, 6776–6785. [CrossRef] [PubMed]
59. Azemtsop Matanfack, G.; Taubert, M.; Guo, S.; Bocklitz, T.; Küsel, K.; Rösch, P.; Popp, J. Monitoring deuterium uptake in single bacterial cells via two-dimensional Raman correlation spectroscopy. *Anal. Chem.* **2021**, *93*, 7714–7723. [CrossRef] [PubMed]
60. Papageorgiou, M.; Tselios, C.; Varotsis, C. Photosensitivity responses of *Sagittula stellata* probed by FTIR, fluorescence and Raman microspectroscopy. *RSC Adv.* **2019**, *9*, 27391–27397. [CrossRef]
61. He, M.; Wu, T.; Pan, S.; Xu, X. Antimicrobial mechanism of flavonoids against *Escherichia coli* ATCC 25922 by model membrane study. *Appl. Surf. Sci.* **2014**, *305*, 515–521. [CrossRef]
62. Gardikis, K.; Hatziantoniou, S.; Viras, K.; Wagner, M.; Demetzos, C. A DSC and Raman spectroscopy study on the effect of PAMAM dendrimer on DPPC model lipid membranes. *Int. J. Pharm.* **2006**, *318*, 118–123. [CrossRef]

63. Germond, A.; Ichimura, T.; Horinouchi, T.; Fujita, H.; Furusawa, C.; Watanabe, T.M. Raman spectral signature reflects transcriptomic features of antibiotic resistance in *Escherichia coli*. *Comm.Biol.* **2018**, *1*, 85. [CrossRef]
64. Wen, Z.Q.; Cao, X.; Vance, A. Conformation and side chains environments of recombinant human interleukin-1 receptor antagonist rh-IL-1ra, probed by Raman, Raman optical activity, and UV-resonance Raman spectroscopy. *J. Pharm. Sci.* **2008**, *97*, 2228–2241. [CrossRef]
65. Jayan, H.; Pu, H.; Sun, D.W. Analyzing macromolecular composition of E. Coli O157: H7 using Raman-stable isotope probing. *Spectrochim. Acta Part A* **2022**, *276*, 121217. [CrossRef]
66. Feng, J.; De La Fuente-Núñez, C.; Trimble, M.J.; Xu, J.; Hancock, R.E.; Lu, X. An in situ Raman spectroscopy-based microfluidic "lab-on-a-chip" platform for non-destructive and continuous characterization of *Pseudomonas aeruginosa* biofilms. *Chem. Comm.* **2015**, *51*, 8966–8969. [CrossRef]
67. Gennis, R.B. The cytochromes of *Escherichia coli*. *FEMS Microbiol. Rev.* **1987**, *3*, 387–399. [CrossRef]
68. Thöny-Meyer, L.; Fischer, F.; Künzler, P.; Ritz, D.; Hennecke, H. Escherichia coli genes required for cytochrome c maturation. *J. Bacteriol.* **1995**, *177*, 4321–4326. [CrossRef]
69. Puustinen, A.; Finel, M.; Haltia, T.; Gennis, R.B.; Wikstrom, M. Properties of the two terminal oxidases of *Escherichia coli*. *Biochemistry* **1991**, *30*, 3936–3942. [CrossRef] [PubMed]
70. Uchida, T.; Mogi, T.; Kitagawa, T. Resonance Raman studies of oxo intermediates in the reaction of pulsed cytochrome bo with hydrogen peroxide. *Biochemistry* **2000**, *39*, 6669–6678. [CrossRef]
71. Laucks, M.L.; Sengupta, A.; Junge, K.; Davis, E.J.; Swanson, B.D. Comparison of psychro-active arctic marine bacteria and common mesophillic bacteria using surface-enhanced Raman spectroscopy. *Appl. Spectrosc.* **2005**, *59*, 1222–1228. [CrossRef]
72. Rastogi, S.K.; Jabal, J.; Zhang, H.; Haler, K.J.; Gibson, C.M.; Qiang, Y.; Branen, A.L. Silica coated Magnetic Nanoparticles SMNPs): Capture and Identification of *Escherichia coli* Cells using surface-enhanced Raman Spectroscopy. *NSTI-Nanotech* **2011**, *2011*, 3.
73. Predoi, D.; Iconaru, S.L.; Albu, M.; Petre, C.C.; Jiga, G. Physicochemical and antimicrobial properties of silver-doped hydroxyapatite collagen biocomposite. *Polym. Eng. Sci.* **2017**, *57*, 537–545. [CrossRef]
74. Bai, W.; Zhao, K.S.; Asami, K. Dielectric properties of *E. coli* cell as simulated by the three-shell spheroidal model. *Biophys. Chem.* **2006**, *122*, 136–142. [CrossRef]
75. Asami, K.; Hanai, T.; Koizumi, N. Dielectric analysis of *Escherichia coli* suspensions in the light of the theory of interfacial polarization. *Biophys. J.* **1980**, *31*, 215–228. [CrossRef] [PubMed]